Document Version: Accepted author manuscript. Published in: IEEE Transactions on Industrial Electronics
DOI: 10.1109/TIE.2019.2952822

Minimum-Loss Control Strategy for a Dual-VSI DFIG DC system

A Gil D. Marques, *Senior Member, IEEE,* Sérgio M. A. Cruz, *Senior Member, IEEE,*
and Matteo F. Iacchetti, *Senior Member, IEEE*

***Abstract* — This paper addresses the minimum-loss control of the Dual-VSI DFIG system connected to a dc link. The minimum-loss operating conditions for field-oriented control based on the airgap flux are obtained analytically using Lagrange multipliers and validated with numerical optimization. As the main contribution of the paper, the analysis accounts for core and VSI losses, providing the optimal stator frequency law and rotor/stator d-axis current split ratio, and an implicit expression for the optimal flux trajectory formulated as equality between suitable d-axis and q-axis loss functions. In the proposed implementation, this implicit condition is enforced by using a proportional-integral controller and avoiding look-up tables. Furthermore, the stator and rotor VSI controls are implemented in two independent DSPs with no communication, which may ease the use of off-the-shelf VSI units. The optimal conditions and control strategy are fully validated by simulations and experiments on a prototype. The main scope of application is wind-energy dc-grid technology.**

***Index Terms*— DFIG, Dc power system, Field-weakening, Efficiency improvement, Dual-VSI DFIG.**

NOMENCLATURE

General

e, E	Dynamical, steady-state electromotive force (p.u.).
$\boldsymbol{f_{sw}}$	VSI Switching frequency.
i, I	Dynamical, steady-state stator, rotor current (p.u.).
$\boldsymbol{I_{md}}$	Magnetizing current (p.u.).
$\boldsymbol{I_{mq}}$	Core loss representing current (p.u.).
$\boldsymbol{L_s, L_m}$	Stator and mutual inductance (p.u.).
$\boldsymbol{L_{ks}, L_{kr}}$	Stator, rotor leakage inductance (p.u.).
P	Active power (p.u.).
$\boldsymbol{P_{se0}}, \boldsymbol{P_{re0}}$	Stator, rotor eddy current loss at standstill (p.u.).
$\boldsymbol{P_{sh0}}, \boldsymbol{P_{rh0}}$	Stator, rotor hysteresis loss at standstill (p.u.).
$\boldsymbol{P_{inv0}}$	Voltage source inverter loss at rated current (p.u.).
$\boldsymbol{P_{sj0}}, \boldsymbol{P_{rj0}}$	Stator, rotor Joule loss at rated current (p.u.).
$\boldsymbol{P_t}$	Total losses.
$P_{d\text{-}axis}, P_{q\text{-}axis}$	Ancillary d- and q-axis loss functions (p.u.).
s	Slip.
$\boldsymbol{T_L}, \boldsymbol{T_e}$	Load, Electromagnetic torque (p.u.).
u, U	Dynamical, steady-state voltage (p.u.).

I. INTRODUCTION

In the last two decades, the Doubly-Fed Induction Generator (DFIG) has been a popular choice for wind energy conversion systems interfaced with the ac mains, due to the significant savings in the power converter – usually rated to 30% of the overall wind energy conversion system (WECS) power [1]. With the growing interest towards dc transmission and distribution systems – especially for wind farm interconnection [2] and dc microgrids [3]-[4], researchers have started looking at the options and benefits of integrating a DFIG into a dc power network. A simple solution to minimize the number of controlled converters and their power rating is the so-called DFIG-DC system. It adopts only a single, de-rated voltage-source inverter (VSI) on the rotor side and a fully-rated diode bridge on the stator, both connected to the same dc-link or dc grid [5]. This scheme effectively implements the cheapest power electronics while allowing high dynamic control and some degree of freedom to optimize losses, but suffers from some severe drawbacks such as harmonic-related extra losses and torque-ripple. Although the torque-ripple can be mitigated at the control level [6], torque-ripple and harmonic compensation cannot be achieved simultaneously [7], without adding extra hardware such as active filters or multi-pulse rectifiers. In order to improve the DFIG-DC system, Nian *et al.* [8] proposed to replace the diode-bridge with a stator-side VSI and operate the DFIG with a slip equal to -1, then realizing a dual-VSI DFIG-DC system where both the VSIs convert half of the total power. The dual-VSI topology for wound-rotor induction machines was explored in the past for high-power motor drive applications in order to achieve a 2-p.u. speed range and using converters rated to 1 p.u. [9]-[13]. This inherent modularity is attractive for multi-MW wind turbines where a larger speed-range can also improve the amount of yearly energy harvested.

The preferred control techniques for the dual-VSI system include vector control [9], dual direct torque control – i.e. acting on rotor and stator windings [10]-[11], and field-oriented control (FOC) or direct torque control (DTC) on one side, combined with V/Hz scalar control on the other side [12]. Techniques based on V/Hz control adopt frequency profiles ensuring a minimum frequency around ten Hz in order to reduce the impact of the winding resistance on the flux estimation [13]. In dual-VSI DFIMs, the errors in the applied stator and rotor voltages cause flux and torque ripple: mitigation techniques using suited PWM combinations are studied in [14].

The FOC based on the airgap flux proposed in [8] for the dual-VSI DFIG-DC system simply forces zero reactive

G. D. Marques is with the INESC-ID, Instituto Superior Técnico (IST), Universidade de Lisboa, Av. Rovisco Pais, no 1, 1049-001 Lisbon, Portugal (e-mail: gil.marques@tecnico.ulisboa.pt).

S. M. A. Cruz is with the Department of Electrical and Computer Engineering, University of Coimbra, and with Instituto de Telecomunicações, Pólo 2 - Pinhal de Marrocos, P-3030-290 Coimbra, Portugal, (e-mail: smacruz@ieee.org).

M. F. Iacchetti is with the Department of Electrical and Electronic Engineering, The University of Manchester, Manchester, M13 9PL, U.K. (e-mail: matteo.iacchetti@manchester.ac.uk).

power at the stator VSI. However, according with some early work on classic ac-grid connected DFIGs, the stator and rotor magnetizing current sharing could be optimized to minimize losses. Optimal conditions for minimum copper losses were formulated in [15]-[16], and the analysis was extended in [17] to include the converter losses as well in the optimization. These results can be generalized to the dual-VSI topology. Furthermore, in DFIG-DC systems, the stator frequency is not constrained to a specific value and provides an extra degree of freedom for the minimization of losses. This opportunity was first recognized in doubly-fed induction motor drives with V/Hz control [18], but the analysis was limited to numerical optimization. Marques *et Al.* [19] derived and tested analytical optimal conditions for the overall losses in the DFIG-DC system, showing that at low and moderate torque the optimal stator flux level drops below the rated value then causing the stator frequency to increase. In [20], the principle was extended to a predictive torque control scheme based on the rotor flux and combined with a compensation strategy for the torque ripple.

Yan *et Al.* [21] looked at a rotor-flux-oriented control of the dual-VSI DFIG-DC system and formulated the optimal rotor flux trajectory minimizing Joule losses up to moderate torque levels. At high torque, the stator-VSI switches to a constant stator voltage and frequency control mode in order not to exceed the rated voltage. In [22], the flux trajectory was modified so as to incorporate a maximum slip frequency constraint. A thorough analysis of the minimum copper loss conditions including all the possible operating constraints was carried out in [23] where five different operating modes were identified and optimal stator and rotor current trajectories were derived. None of these previous studies, however, paid attention to core and converter losses which can affect quite significantly the optimal conditions.

This paper presents a novel optimization analysis and control implementation for the dual-VSI DFIG-DC system and incorporates the following major novelties:

- It includes the effects of core and conduction losses in the two VSIs, in order to minimize the overall system losses.
- It derives an optimal stator frequency versus speed profile, thereby moving away from a stator/rotor active power split set *a priori* [23].
- As an explicit optimal flux trajectory cannot be derived in closed form, the proposed scheme enforces the implicit optimal conditions via a proportional-integral (PI) controller, then avoiding using look-up tables.

The paper is organized as follows. Section II presents the modelling background, whereas Section III introduces the formulation for the optimization problem. The analytic optimization based on Lagrange multipliers is carried out in Section IV by using simplified expressions for the constraints and losses. The results are validated with numerical optimization in Section V, which assesses the impact of the approximations. Section VI explains the implementation aspects for the proposed real-time control tracking the optimal frequency, flux and currents. Finally, Section VII presents the experimental validation.

II. DUAL-VSI DFIG-DC SYSTEM STEADY-STATE MODEL

Minimum-loss control-strategies are used to save energy. During fast transients, the minimum loss operation is not achieved but the additional energy loss is low and not very significant, if the transient is short. Thus, only steady-state or slow transient regimens are interesting in the study, as assumed also in [15]-[23], [25].

The Dual-VSI DFIG-DC system is shown in Fig. 1. The wound-rotor induction machine (WRIM) T-equivalent circuit for steady-state analysis is shown in Fig. 2. The total core losses are represented with a current source in parallel with the magnetizing inductance: the value of I_{mq} is computed from the expression of core losses as function of airgap flux, stator frequency and rotor or slip frequency [19]. The analysis in this paper adopts per-unit p.u. variables and motoring conventions for stator and rotor terminals and for torque.

As shown in Section IV, for power generation applications the minimum-loss operation requires negative slip values close to -1. Consequently, with the conventions of Fig. 2, the stator and rotor voltage phasors are almost in opposition with each other and the relevant vector diagram is as in Fig. 3, where the d- and q-axis definition considers airgap-flux orientation. The d-axis stator and rotor current components are both positive as the total magnetizing power is shared by both stator and rotor VSIs according to the minimum loss condition. This is convenient from the point of view of the system design.

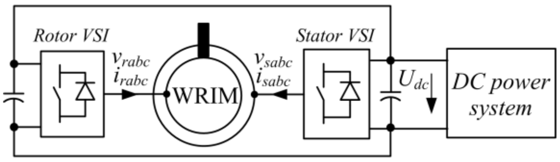

Fig. 1. System layout and general control scheme.

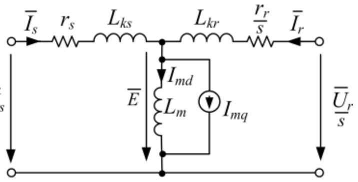

Fig. 2 Equivalent circuit of the induction machine.

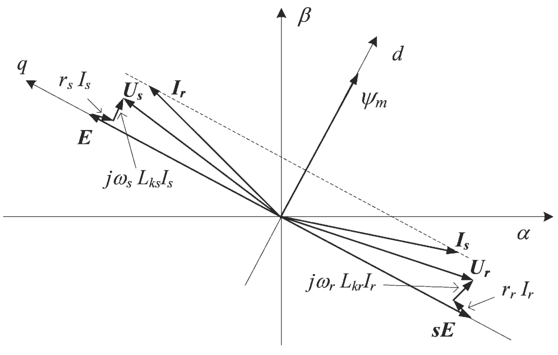

Fig. 3 Simplified steady-state phasor diagram for negative slip (s= -1) and generating operation. Airgap flux orientation. (I_{mq} is omitted)

Under airgap flux orientation, the equivalent circuit of Fig. 2 is described by the following steady-state equations:

$$\bar{U}_s - r_s\bar{I}_s - j\omega_s L_{ks}\bar{I}_s = j\omega_s\bar{\psi}_m \tag{1}$$

$$\frac{\bar{U}_r}{s} = j\omega_s\bar{\psi}_m + \frac{r_r}{s}\bar{I}_r + j\omega_s L_{kr}\bar{I}_r \tag{2}$$

$$\bar{I}_s + \bar{I}_r = I_{md} + jI_{mq} \tag{3}$$

Current I_{mq} represents total core losses P_{fe}, according with:

$$P_{fe} = EI_{mq} = \omega_s\psi_m I_{mq} \tag{4}$$

$$\omega_r = s\omega_s = \omega_s - \omega_m\ . \tag{5}$$

A. Losses in the Dual-VSI DFIG-DC system

Considering a steady-state operating point at rotor speed ω_m and torque T_L, the losses in the Dual-VSI DFIG-DC system can be expressed using p.u. variables as follows:

Stator Joule losses $$P_{js} = r_s I_s^2 = P_{sj0} I_s^2 \tag{6}$$

Rotor Joule losses $$P_{jr} = r_r I_r^2 = P_{rj0} I_r^2 \tag{7}$$

Stator-VSI losses $$P_{inv_s} = P_{inv_{s0}}\, I_s \tag{8}$$

Rotor VSI losses $$P_{inv_r} = P_{inv_{r0}}\, I_r \tag{9}$$

Equations (8)-(9) assume a simplified model with constant voltage drop across switches, to be calculated from the device characteristics. The differential resistance can be lumped into the winding resistance. Switching losses for constant dc voltage and switching frequency are roughly proportional to the current magnitude (see Appendix II) and are inherently incorporated in (8) and (9) [17].

Core losses mainly include eddy current and hysteresis losses. In this paper, a simplified methodology to represent the core losses in WRIMs is used [24]. Stator and rotor eddy current losses are proportional to the squared flux and to the square of stator and slip frequency respectively. Stator and rotor hysteresis losses are considered proportional to the flux squared to the frequency and slip frequency respectively. In p.u. they are as follows:

$$P_{sh} = P_{sh0}\omega_s\psi_m^2 \tag{10}$$

$$P_{se} = P_{se0}\omega_s^2\psi_m^2 \tag{11}$$

$$P_{rh} = P_{rh0}|\omega_r|\,\psi_m^2 \tag{12}$$

$$P_{re} = P_{re0}\omega_r^2\psi_m^2 \tag{13}$$

These give a more accurate representation of core losses compared to the constant-resistor model [25]. Based on [24] (10)-(13), the core losses for negative slip are given by:

$$P_{fe} = \psi_m^2 f(\omega_s, \omega_m) = \psi_m^2 \begin{Bmatrix} P_{sh0}\omega_s + P_{rh0}(\omega_m - \omega_s) + \\ P_{se0}\omega_s^2 + \ P_{re0}\,(\omega_m - \omega_s)^2 \end{Bmatrix} \tag{14}$$

Function $f(\omega_s, \omega_m)$ is defined in order to simplify the analysis that will be presented in Section III. The core-loss equivalent current I_{mq} in Fig. 2 can then be evaluated as:

$$I_{mq} = \frac{\psi_m f(\omega_s,\omega_m)}{\omega_s}. \tag{15}$$

B. Torque expression

Rotor core losses produce parasitic torque components, which can be found by dividing rotor core losses by the slip frequency. The torque component due to rotor hysteresis losses urges the rotor in the direction of the rotating field seen from the rotor: it has roughly constant magnitude and changes sign when the rotor speed crosses the synchronous value [24]. The parasitic torque due to eddy currents is proportional to the slip frequency and has a braking effect.

Under motoring conventions and assuming a negative slip as in the proposed optimal control, the torque is given by [24]:

$$T_e = -\psi_m I_{rq} + P_{reo} s\omega_s\psi_m^2 - P_{rh0}\psi_m^2 \tag{16}$$

The second and third term in (16) are associated with rotor eddy current and hysteresis core losses respectively.

III. OPTIMIZATION PROBLEM FORMULATION

The analysis in this paper looks at the optimal control variables which minimize losses for a given speed and torque, when the system is operating in generating mode.

The objective function is the expression of the total losses (neglecting mechanical losses):

$$W = \begin{Bmatrix} \psi_m^2 f(\omega_s,\omega_m) + r_s\left(I_{sd}^2 + I_{sq}^2\right) + r_r\left(I_{rd}^2 + I_{rq}^2\right) \\ +P_{inv_{s0}}\, I_s + P_{inv_{r0}}\, I_r \end{Bmatrix} \tag{17}$$

When compared with a classic DFIG with the stator connected to the ac mains, the stator voltage and frequency in the DFIG-DC system provide additional degrees of freedom, which can be used to optimize the operation. The problem formulation considers the following constraints:

1) Equality constraints:

$$T_e = T_L \tag{18}$$

$$\psi_m = L_m(I_{sd} + I_{rd}) \tag{19}$$

$$I_{mq} = \left(I_{sq} + I_{rq}\right) \tag{20}$$

2) Inequality constraints:

$$I_r = \sqrt{I_{rd}^2 + I_{rq}^2} \le I_{rN} \tag{21}$$

$$I_s = \sqrt{I_{sd}^2 + I_{sq}^2} \le I_{sN} \tag{22}$$

$$U_s = \sqrt{U_{sd}^2 + U_{sq}^2} \le U_{sN} \tag{23}$$

$$U_r = \sqrt{U_{rd}^2 + U_{rq}^2} \le U_{rN} \tag{24}$$

$$\psi_{min} \le \psi_m \le \psi_{max} \tag{25}$$

$$\omega_s \le \omega_{s_{max}} \tag{26}$$

$$\omega_r \le \omega_{r_{max}} \tag{27}$$

The solution of this optimization problem can be obtained using several methods. In Sect. IV, the Lagrange optimization method is used to obtain simplified expressions useful to devise a control method for the system. In Section V, numerical methods are used to verify and extend the simplified results. For the theoretical analysis of the impact of constraints, it is assumed that the WRIM is designed using the optimality conditions found in this work, in such a way as to trigger stator and rotor constraints simultaneously and maximize the unconstrained operating region.

IV. ANALYTICAL OPTIMIZATION

In order to obtain analytic results in a compact form for the control implementation, the parasitic torque components due to rotor core losses are neglected in (16) and the constraint (20) is simplified into $I_{rq} \approx -I_{sq}$ (i.e. $I_{mq} \approx 0$). This leads to a small error in the calculation of the optimal I_{rq} and I_{sq} . The incremental Joule and VSI losses due to the circulation of I_{mq} are neglected. Rotor core losses are still considered in (17) but not in (18). Even with these approximations, an explicit closed-form solution for the optimal values of all variables cannot be obtained, unless

VSI losses are neglected. Nonetheless, the practical control implementation can handle optimal conditions in an implicit form, considering that some quantities such as current components and magnitudes are measured or estimated in real-time. The results obtained in this section are verified numerically in section V.

A. Unconstrained optimization by Lagrange Multipliers

The simplified Lagrange function including (17)-(20) is:

$$W_L \approx \left\{ \begin{array}{c} \psi_m^2 f(\omega_s, \omega_m) + r_s\left(I_{sd}^2 + I_{sq}^2\right) + r_r\left(I_{rd}^2 + I_{rq}^2\right) + \\ P_{inv_{s0}}\sqrt{I_{sd}^2 + I_{sq}^2} + P_{inv_{r0}}\sqrt{I_{rd}^2 + I_{rq}^2} - \lambda_3\left(I_{sq} + I_{rq}\right) \\ -\lambda_1\left(T_L + \psi_m I_{rq}\right) - \lambda_2\left(\psi_m - L_m(I_{sd} + I_{rd})\right) \end{array} \right\} \quad (28)$$

The three Lagrange multipliers $\lambda_{1,2,3}$ introduce the equality constraints (18)-(20). The inputs and optimization variables are $\{\omega_m, T_L\}$ and $\{\omega_s, I_{sd}, I_{sq}, I_{rd}, I_{rq}, \psi_m, \lambda_1, \lambda_2, \lambda_3\}$.

1) Optimal stator frequency

In the simplified formulation, the stator and rotor frequency only affect core losses and do not have direct influence on the torque, semiconductor and Joule loss expressions as well as on the relation between airgap flux and d-axis currents. Since ω_s appears only in the first term of W_L in (28), the optimal condition for ω_s is:

$$\frac{\partial W_L}{\partial \omega_s} = \psi_m^2 \frac{\partial f(\omega_m, \omega_s)}{\partial \omega_s} = 0 \quad (29)$$

From (29) and (14) it can be concluded that the first minimum-loss condition is obtained when the partial derivatives of stator and rotor core losses with respect to ω_s are equal to each other. Factor ψ_m^2 in (29) can be eliminated, which means that (29) is still valid when the maximum flux constraint is active. Expanding the partial derivative in (29) by using (14) and solving (29) for ω_s gives the following optimal stator frequency vs speed profile

$$\omega_s = \frac{P_{re0}}{(P_{se0} + P_{re0})}\omega_m - \frac{P_{sh0} - P_{rh0}}{2(P_{se0} + P_{re0})} \quad (30)$$

Equation (30) represents a straight line with the slope determined by the weight of rotor and total eddy current losses and can be used directly as a control law. This formula is also valid when the flux is limited by the constraint (25). Rotor or stator voltage constraints, however, can slightly change the optimal value of ω_s: this aspect is tackled in Section V using numerical methods. Compared to $\omega_s = \omega_m/2$ (i.e. *slip* =-1) adopted in [8], the optimal ω_s (30) has still a linear trend but depends on core loss parameters, that introduce a small offset and slope change.

2) Optimal magnetizing current split condition.

The optimal conditions for the currents in (28) are:

$$\frac{\partial W_L}{\partial I_{sd}} = 2r_s I_{sd} + \frac{P_{inv_{s0}} I_{sd}}{\sqrt{I_{sd}^2 + I_{sq}^2}} + \lambda_2 L_m = 0 \quad (31)$$

$$\frac{\partial W_L}{\partial I_{sq}} = 2r_s I_{sq} + \frac{P_{inv_{s0}} I_{sq}}{\sqrt{I_{sd}^2 + I_{sq}^2}} - \lambda_3 = 0 \quad (32)$$

$$\frac{\partial W_L}{\partial I_{rd}} = 2r_r I_{rd} + \frac{P_{inv_{r0}} I_{rd}}{\sqrt{I_{rd}^2 + I_{rq}^2}} + \lambda_2 L_m = 0 \quad (33)$$

$$\frac{\partial W_L}{\partial I_{rq}} = 2r_r I_{rq} + \frac{P_{inv_{r0}} I_{rq}}{\sqrt{I_{rd}^2 + I_{rq}^2}} - \lambda_1 \psi_m - \lambda_3 = 0 \quad (34)$$

Eliminating λ_2 from (31) and (33) gives the second optimal minimum loss condition:

$$2r_s I_{sd} + \frac{P_{inv_{s0}} I_{sd}}{\sqrt{I_{sd}^2 + I_{sq}^2}} = 2r_r I_{rd} + \frac{P_{inv_{r0}} I_{rd}}{\sqrt{I_{rd}^2 + I_{rq}^2}} \quad (35)$$

If VSI losses are neglected, (35) states that the resistive voltage drops due to stator and rotor d-axis current components must be equal to each other for the losses to be minimized. This coincides with the condition for minimum-Joule-loss-operation derived in [23] for the dual-VSI WRIM as well as in [15] for the classic ac-grid connected DFIG. In the particular case of "balanced" machine and VSIs – i.e. equal rotor and stator p.u. parameters and losses, the system should be operated with identical stator and rotor d-axis currents. In the general case, (35) can be rewritten as follows

$$I_{rd} = \left(\left(r_s + \frac{P_{inv_{s0}}}{2\sqrt{I_{sd}^2 + I_{sq}^2}}\right) \Big/ \left(r_r + \frac{P_{inv_{r0}}}{2\sqrt{I_{rd}^2 + I_{rq}^2}}\right)\right) I_{sd} \quad (36)$$

Lagrange multipliers λ_2 and λ_3 are immediately obtained by solving (33) and (32) respectively.

$$\lambda_2 = -\frac{2r_r}{L_m} I_{rd} - \frac{P_{inv_{r0}}}{L_m} \frac{I_{rd}}{\sqrt{I_{rd}^2 + I_{rq}^2}} \quad (37)$$

$$\lambda_3 = 2r_s I_{sq} + \frac{P_{inv_{s0}} I_{sq}}{\sqrt{I_{sd}^2 + I_{sq}^2}} \quad (38)$$

Replacing (38) into (34) and solving with respect to λ_1 gives

$$\lambda_1 = \left(2r_r + \frac{P_{inv_{r0}}}{\sqrt{I_{rd}^2 + I_{rq}^2}}\right) \frac{I_{rq}}{\psi_m} - \left(2r_s + \frac{P_{inv_{s0}}}{\sqrt{I_{sd}^2 + I_{sq}^2}}\right) \frac{I_{sq}}{\psi_m} \quad (39)$$

3) Optimal airgap flux condition.

As (28) contains only a quadratic and two linear terms with ψ_m, the optimal condition for ψ_m in (28) is:

$$\frac{\partial W_L}{\partial \psi_m} = 2\psi_m f(\omega_m, \omega_s) - \lambda_1 I_{rq} - \lambda_2 = 0 \quad (40)$$

After some manipulations and assuming $I_{mq} = 0$ (i.e. $I_{rq} \approx -I_{sq}$) (40) leads to the third minimum-loss condition (42) at the bottom of the page. Equation (42) tells that the optimal flux value makes ancillary functions P_{d-axis} and P_{q-axis} defined by the left and right hand side of (42) are equal to each other. If VSI losses are neglected, (42) takes the much more compact form (41)

$$\psi_m^2 f(\omega_m, \omega_s) + r_s I_{sd}^2 + r_r I_{rd}^2 = r_s I_{sq}^2 + r_r I_{rq}^2 \quad (41)$$

$$\underbrace{\psi_m^2 f(\omega_m, \omega_s) + \left(r_r + \frac{P_{inv_{r0}}/2}{\sqrt{I_{rd}^2 + I_{rq}^2}}\right) I_{rd}^2 + \left(r_s + \frac{P_{inv_{s0}}/2}{\sqrt{I_{sd}^2 + I_{sq}^2}}\right) I_{sd}^2}_{P_{d-axis}} = \underbrace{\left(r_r + \frac{P_{inv_{r0}}/2}{\sqrt{I_{rd}^2 + I_{rq}^2}}\right) I_{rq}^2 + \left(r_s + \frac{P_{inv_{s0}}/2}{\sqrt{I_{sd}^2 + I_{sq}^2}}\right) I_{sq}^2}_{P_{q-axis}} \quad (42)$$

The sums in the left-hand and right-hand sides of (41) represent torque-independent (magnetization-related) and torque-dependent losses respectively. As stated by (41), the airgap flux should be adjusted by the control system in order to force these two terms to match.

B. Effect of constraints

The operating modes of a dual-VSI WRIM have been thoroughly analyzed in [23] identifying the sequence in which the constraints are triggered. This Section revises the optimal trajectories and constraints for the optimization including core and VSI losses. The discussion will focus on a balanced WRIM, as this is the most natural design condition for a FOC based on the airgap flux.

For speed values up to 2 p.u. only the flux and current constraints are relevant. In this region, the optimal flux from the implicit condition (42) increases with torque until reaching the rated value. For higher torque levels, the flux is to be capped at the rated value, while the optimal frequency profile (30) and d-axis current sharing condition (36) are still valid because they are independent of the flux. Eventually, the stator and rotor current reach the rated value and the torque cannot be increased further. Fig. 4 refers to a benchmark symmetric WRIM derived from the machine in the Appendix by making the stator parameters identical to the rotor ones.

Fig. 4 compares the optimal stator current trajectories in the $i_{sd} - i_{sq}$ plane including VSI and core losses (black line) and only considering winding Joule losses (brown line) – according to [23]. Both trajectories ramp up from the origin to the flux saturation point and then become vertical up to the rated point at the intersection of stator (thick, red) and rotor (thick, dashed, blue) current limit circles.

The center of the rotor current limit circle $I_{rd}^2 + I_{rq}^2 = I_{rN}^2$ is located at $I_{sd} = \psi_m / L_m$ according to (19), (20) with $I_{mq} \approx 0$. Thus, the center moves rightwards as torque and flux increase, but Fig. 4 only shows the final position at rated flux (at I_{sd}=0.642 p.u., with the WRIM parameters in the Appendix). The trajectory with VSI and core losses (black) is significantly much steeper than the linear trajectory (brown) predicted by [23], as evidence that the increasing torque is achieved by prioritizing I_{sq} on ψ_m, in order to keep core losses limited.

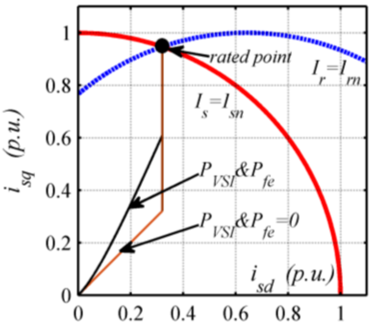

Fig. 4 Optimal stator current trajectories for speeds up to 2 p.u. value, in a symmetric WRIM (same stat. and rot. param.).

As mentioned in Section IV-A-3), condition (42) defines implicitly the optimal flux level when the system is operating within the flux, current and voltage limits. Above 2 p.u. speed, the flux must be reduced in order to meet the voltage constraints. With low or moderate torque levels, the optimal flux implicitly defined by (42) may still comply with voltage constraints (23)-(24). In a balanced WRIM, (30) and (36) reduce to $\omega_s = \omega_m/2$ and $I_{sd} = I_{rd} = \psi_m / 2L_m$ respectively, similarly to the control strategy proposed in [8]. This ensures that the stator and rotor voltage constraints are triggered simultaneously. The condition for the limit flux value is found from the stator or rotor equations (1)-(2) by neglecting the resistive voltage drops

$$U_{sM}^2 \approx \omega_s^2 (\psi_m + L_{ks} I_{sd})^2 + \omega_s^2 L_{ks}^2 I_{sq}^2 \qquad (43)$$

Replacing $\omega_s = \omega_m/2$, $I_{sd} = I_{rd} = \psi_m / 2L_m$ and $I_{sq} = T_L / \omega_m$ into (43) and solving for ψ_m yields the flux limit value ψ_{mU} (44).

$$\psi_{mU} = \frac{2\sqrt{2}L_m}{L_{ks}+2L_m} \sqrt{\left(\frac{U_{sM}}{\omega_m}\right)^2 - \sqrt{\left(\frac{U_{sM}}{\omega_m}\right)^4 - \left(L_{ks}\frac{L_{ks}+2L_m}{4L_m} T_L\right)^2}} \qquad (44)$$

When $\psi_m > \psi_{mU}$ in (44), the control can no longer enforce (42) and there are no degrees of freedom left, as the voltage limits are hit.

V. NUMERICAL OPTIMIZATION RESULTS

The numeric optimization was carried out with Matlab fmincon function with “interior point” method. The program takes less than one second to obtain a solution for each point (speed, torque) using a low-performance computer. Some of the control variables resulting from the numeric optimization are plotted in Fig. 5 to Fig. 11 as a function of inputs $\{\omega_m, T_L\}$.

Fig. 5 presents the optimal stator frequency surface and proves that the optimal stator frequency is almost independent of torque unless voltage or current constraints are active (high T_L and ω_m). Even so, the deviation from the ideal plane is marginal, then proving the validity of (30). This is illustrated in a different way in Fig. 6 comparing the optimal trajectories as extracted from Fig. 5 for different torque values to the approximated analytic trajectory (30) (coincident to the curve for $T_L = 0.35$ p.u.). For low torque and speed, the approximation is excellent. Only at high speed and torque there is a deviation from (30).

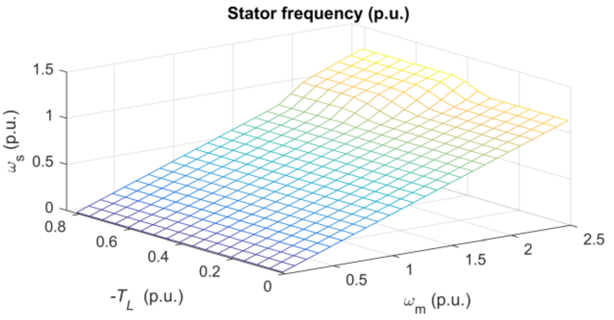

Fig. 5 Stator frequency.

Fig. 7 presents the optimal airgap flux surface and shows that there are four different regions:

A – Minimum flux region: for small torque, when the flux hits the minimum value set at 0.5 p.u..

B – Low torque region: field weakening for reducing core loss – no constraints active; here the optimal flux depends strongly on torque and weakly on speed, as emphasized by the iso-lines in Fig. 8. This figure also shows the “limit curve” corresponding to $(42)_{left\ h.s.} - (42)_{right\ h.s.} = 0$ (dashed red line). It was verified that inside this limit curve, surface

"(42)$_{left\ h.s.}$ - (42) $_{right\ h.s.}$" is squeezed on the plane $\{\omega_m, T_L\}$, i.e. it is almost zero. This proves that, despite the approximations in the analytic optimization, (42) matches with the curves obtained using numeric optimization.

C – Maximum flux region: for high torque and low-medium speeds.

D – Maximum voltage region: voltage constraint (23) and/or (24) active, this is the classic flux weakening region.

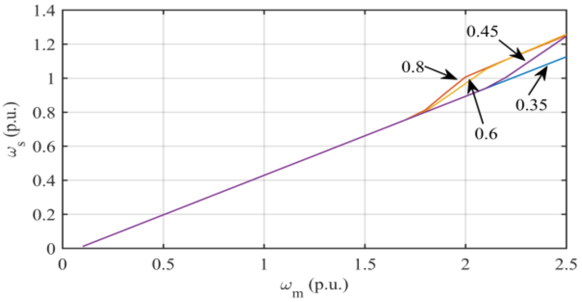

Fig. 6 Optimal stator frequency ω_s versus ω_m for several values of torque $\{0.35, 0.45, 0.6, 0.8\}$, and approximation (30) (coincident with the straight line at $T_L = 0.35$ p.u.).

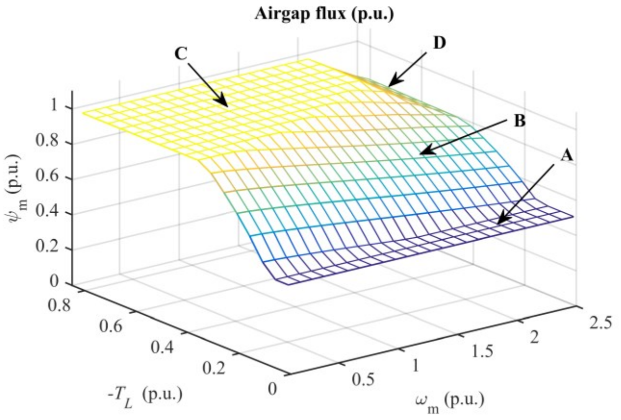

Fig. 7 Airgap flux from numerical optimization.

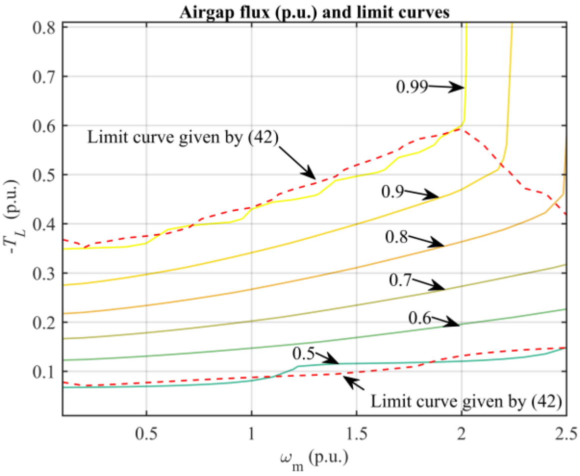

Fig. 8 Constant flux lines on the ω_m-T_L plane obtained using numerical optimization and limit curves obtained by (42).

The rotor voltage and current magnitudes are presented in Fig. 9: similar results are obtained for stator voltage and current, so they are not shown here. The rotor (and stator) current increases with torque as expected: when flux or voltage saturation occurs the current gradient is steeper.

Condition (35) for the optimal d-axis current split is verified in Fig. 10 showing that (35) is valid also when the maximum flux constraint (25) is active. If voltage or current constraints are active, the violation is less than 1%. For high values of torque and speed, the numerical method used does not converge to a feasible solution. This is shown in Fig. 10.

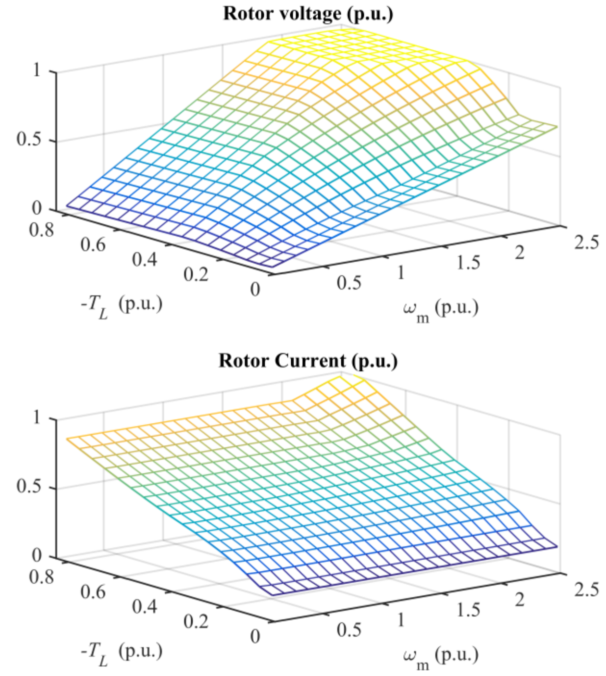

Fig. 9 Rotor voltage and current.

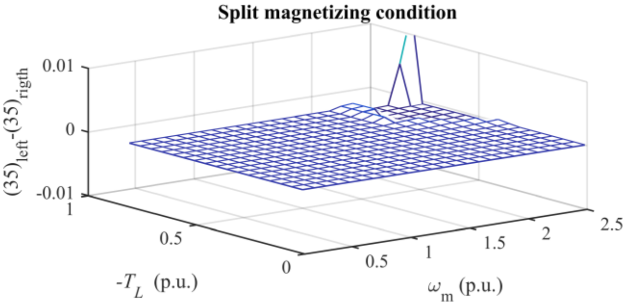

Fig. 10 Difference "(35)$_{\text{left-hand}}$ - (35) $_{\text{right-hand}}$" for the verification of the optimal d-axis split current condition.

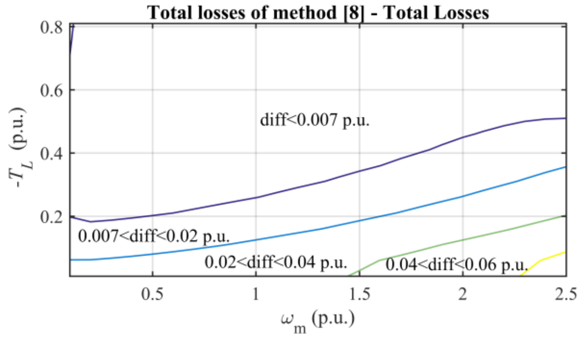

Fig. 11 Contour lines of the difference between total losses with method [8] and with the proposed method.

The benefit of using the proposed control strategy compared to the method in [8] is illustrated in Fig. 11 showing the difference in total losses with the control method [8] and the method presented here. Method [8] was chosen because it adopts a similar FOC on the magnetizing flux, with equal stator/rotor d-axis split and *slip*=-1, but it does not incorporate any loss-optimization functionality. Fig. 11 shows that at high speed and low torque the savings in losses with the proposed method can exceed 0.05 p.u.. In the maximum-flux region, however, the benefit is very small.

The importance of accounting for core and VSI losses in the optimization is illustrated in Fig. 12. This was obtained by running the numerical optimization in two setups and taking the total loss difference between the two. Actual VSI and core loss parameters were used in the first setup. In the second setup, these values were set to zero in optimal conditions (36) and (42), so as to optimize only Joule losses, like in [23]. As (30) is undefined for zero core losses, the optimal stator frequency profile in Fig. 5 was forced also in the second scenario. This choice was deliberate in order to make the benefit (loss reduction) close to the minimum possible so as to challenge the proposed method. Nonetheless, Fig. 12 shows that the maximum total power loss reduction can reach 0.01 p.u. in the unconstrained region at relatively high speed and low torque. It was also verified that using a different frequency rule in order to have a power split far from unity (e.g. 0.7 in [23]) causes the loss difference to increase even above 0.02 p.u. in the high speed - high torque region. This is due to the impact of the higher frequency on core losses in either the rotor or stator laminations.

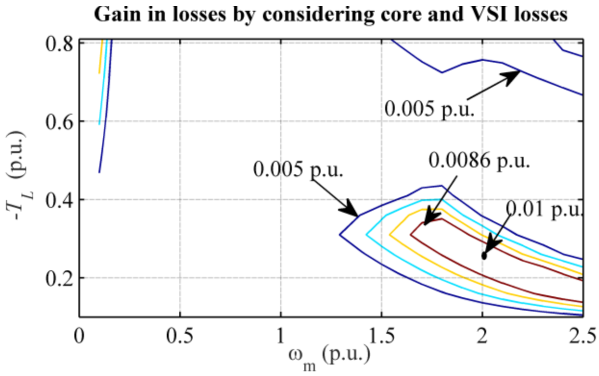

Fig. 12 Contour lines of the difference between total losses with the proposed method ignoring or considering VSI and core losses in the optimization.

VI. CONTROL SYSTEM

Fig. 13 illustrates the implementation of the dual-VSI DFIG-DC FOC aligned with the airgap flux (see Fig. 3) and embedding the simplified optimization methodology presented in Section IV. Stator and rotor VSI are controlled with two independent DSPs with no communication between each other. For this purpose, the airgap flux estimator block is replicated in each DSP by using the flux-current relationship written in the d-q and stator frame respectively, as shown in (45).

$$\begin{aligned}\bar{\psi}_m &= L_m\left(\bar{\imath}_{s\,dq} + \bar{\imath}_{r\,dq}\right)\\ \bar{\psi}_{m\,\alpha\beta} &= L_m\left(\bar{\imath}_{s\,\alpha\beta} + \bar{\imath}_{r\,\alpha\beta}e^{j\gamma_m}\right)\end{aligned} \qquad (45\text{-a,b})$$

The optimal conditions in Section IV are implemented via the stator and rotor converter control as detailed below.

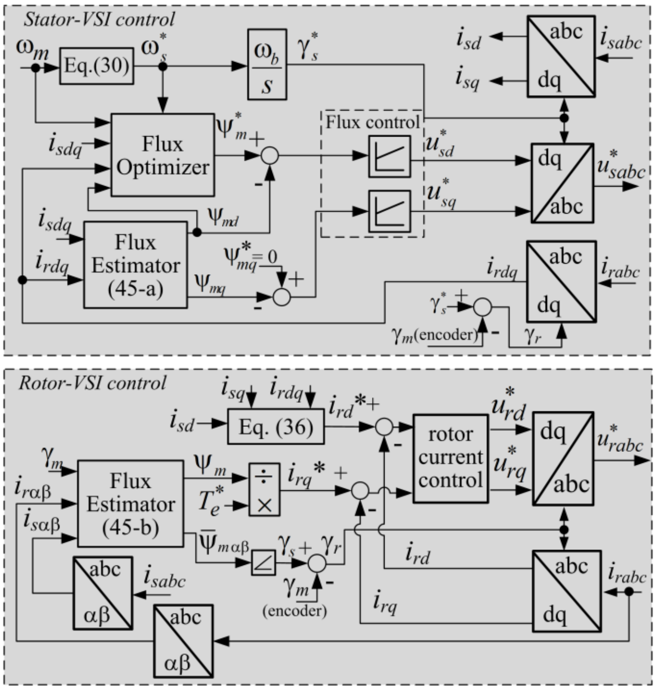

Fig. 13 Control implementation.

The stator VSI is in charge of the optimal stator frequency and airgap flux regulation. The stator frequency control and field orientation are achieved by using the integral of the stator frequency optimal set-point as a stator frame angle and forcing the q-axis airgap flux component in (45-a) to zero via a PI controller. On the d-axis, a PI controller tracks the optimal airgap flux magnitude ψ_m^*. These two PI controllers adjust the stator voltage at the appropriate value. The rotor d-axis current component acts as a disturbance to the flux controller.

The optimal airgap flux reference value $\psi_m^* = \psi_{md}^*$ is determined by the "flux optimizer" block detailed in Fig. 14. This comprises loss calculation blocks and a PI controller implementing the flux saturation. The controller forces the d- and q-axis losses to be identical, as stated in (42). For a given torque level, airgap flux and stator or rotor q-axis currents vary inversely to each other until flux saturation (25) is triggered. Beyond that point, (42) is abandoned.

The rotor VSI regulates the torque and the optimal rotor airgap current using a standard inner-loop current control scheme based on PI controllers [1]. The field orientation in the rotor VSI control is achieved directly by using the slip angle in the frame transformations. This is calculated as a difference between the airgap flux angle – from (45-b), and the encoder angle. The block generating the optimal rotor reference currents is shown in Fig. 13 and is based on (36).

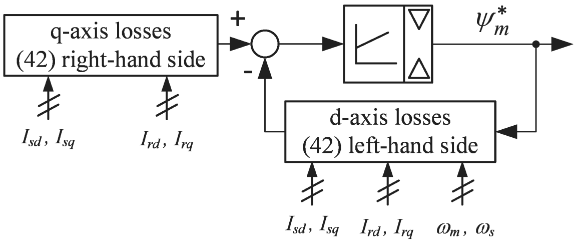

Fig. 14 Airgap flux optimization and control.

VII. EXPERIMENTAL VALIDATION

The theory and the implementation described in this paper are validated using a lab test-rig including a WRIM (see the parameters in the Appendix), and a stator and rotor VSI tied to the 200 V lab dc network. This dc network is fed by a 40 kW dc machine driven by an induction motor. The delta-connected stator needed a 4 kVA 220/110V transformer to equalize stator-VSI and rotor-VSI ac voltage levels. The two VSIs are controlled by two independent, low-cost Microchip fixed point dsPIC30F4011 with no communication between each other. They only share the output of the stator and rotor current sensors and the rotor position encoder (4096-step resolution). The results in real-time come from four 30 kHz PWM output channels per dsPIC, feeding low-pass RC filters with 600 Hz bandwidth. This bandwidth is appropriate for visualization of the transients. As two dsPICs are used, up to eight signals can be recorded simultaneously. The WRIM is driven by a separate excitation dc motor with the armature voltage adjusted by a simple three-phase variac and diode bridge. This causes small rotor speed variations depending on the load. The lower and upper limit of the airgap flux controller in Fig. 14 is set to 0.5 and 0.93 p.u. (rated) respectively.

The VSIs switching frequency is 3 kHz, and the Interrupt Service Routine sampling frequency is 10 kHz. The differential anti-windup implementation was adopted for all PI controllers. The airgap flux controllers and rotor current controllers were designed for a 6 p.u. bandwidth using the ITAE criterion. The PI controller in the flux optimizer (see Fig. 14) was designed using simulation tools and a trial-and-error approach, leading to a 0.6 p.u. bandwidth. A photograph of the experimental setup is shown in Fig. 14.

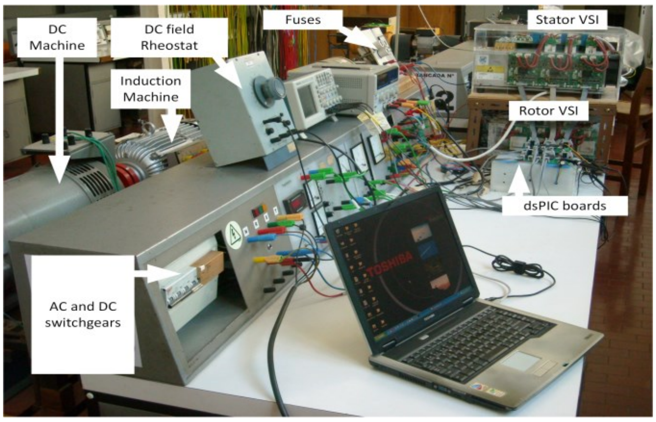

Fig. 15 Experimental setup.

A. Response of the airgap flux dq controllers

The airgap flux control was first tested without using the flux optimization block in Fig. 14, with a step change in the reference ψ_m^* from 0.6 to 0.8 p.u., at t=8 ms and next, in a second transient, with a step on i_{rd}^* that acts as a disturbance on the controller at t=5 ms. Fig. 16 shows the reference step response at zero rotor currents (i.e. rotor VSI disconnected) and the disturbance response when a step on i_{rd}^* is imposed. It shows that when i_{rd} increases i_{sd} decreases accordingly, without significant perturbation on the airgap flux. This validates the implementation of (35).

The traces shown in Fig. 16 are obviously affected by the 600 Hz bandwidth of the RC filters in the output channels, which explain the sluggish appearance of ψ_m^*.

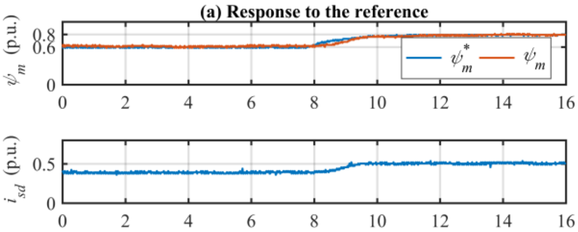

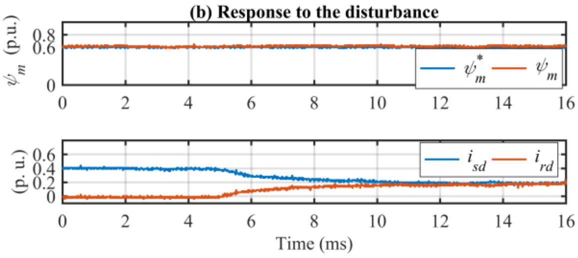

Fig. 16 Airgap flux controller response. (a) After a step in the reference ψ_m^*; (b) After a step in the “disturbance” i_{rd}^*.

B. Open-loop response to a decreasing flux ramp

Fig. 17 proves the soundness of (42) by showing the trend of d-, q-axis ancillary functions, and total losses at constant-torque (0.2 p.u.) operation at $\omega_m = 1.0\,p.u.$, when the airgap flux optimization block in Fig. 14 is disabled and the flux is decreased from its rated value (0.93 p.u.) down to 0.5 p.u.. The total losses are minimum when the two loss components are equal, as from (42).

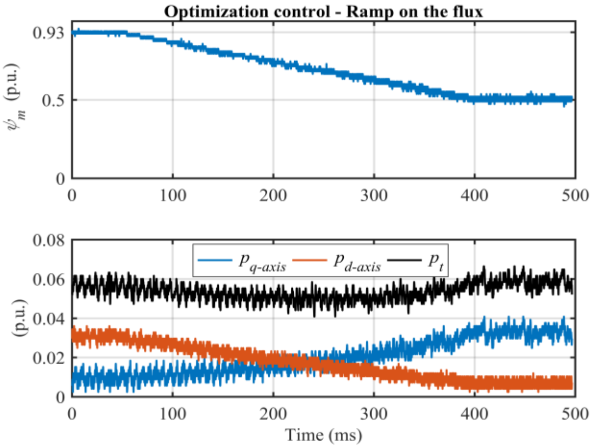

Fig. 17 Behavior of losses when the flux is decreased.

C. Closed-loop operation using the flux controller

Fig. 18 and Fig. 19 show the response of the control to a step with two different values on the torque reference with the flux optimizer block enabled in order to force the optimal condition (42).

Fig. 18 and Fig. 19 prove that at lower torque, the control forces a lower optimal flux and smaller values for the ancillary loss functions $P_{d\text{-}axis}$ and $P_{q\text{-}axis}$ are obtained. This is in accordance with Fig. 8. The d-axis current split condition (36) is determined by the stator and rotor resistance ratio r_s/r_r=1.2 and the VSI losses that depend on the operating point. The inclusion of the VSI losses turns the value of these currents almost equal.

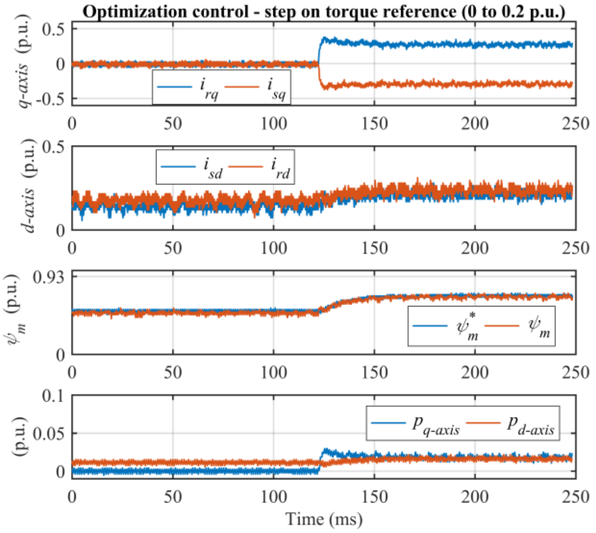

Fig. 18 Response to a torque step to 0.2 p.u. at 1500 rpm.

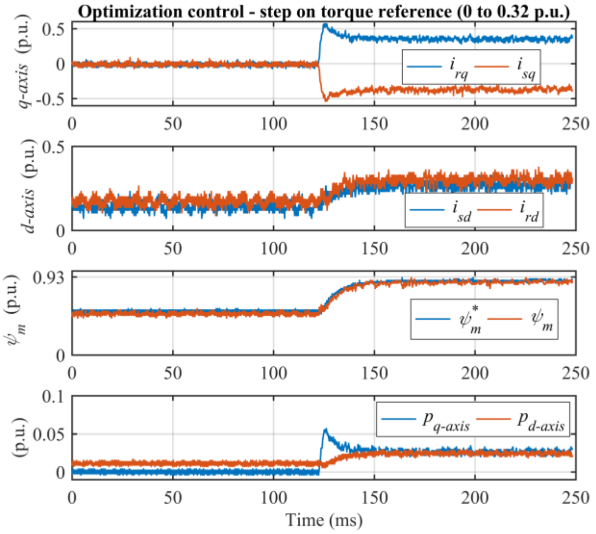

Fig. 19 Response to a torque step to 0.32 p.u. at 1500 rpm.

D. Loss reduction due to flux adjustment

Fig. 20 shows the response to a ramp on the reference torque from zero to 0.40 p.u. in two different conditions. In the first condition – "subscript 1", the flux optimizer in Fig. 13 is active and adjusts the flux level according to Fig. 14. In the second condition – "subscript 2", the flux level is kept at rated value. Fig. 20 proves that the total losses are reduced when the flux is adjusted. The resulting loss savings are aligned with the values presented in Fig. 11. As predicted by the theory, the benefit becomes smaller when the torque level increases.

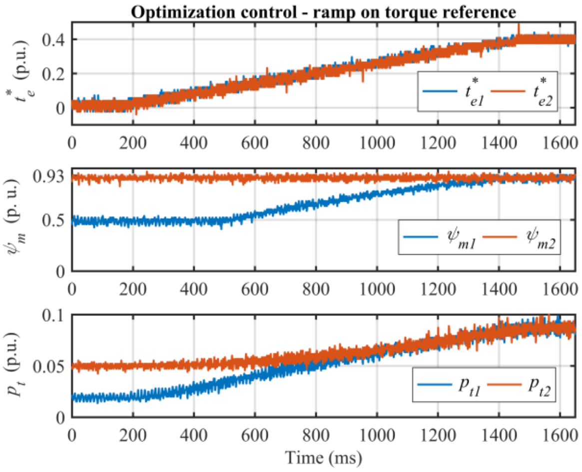

Fig. 20 Response to a ramp on the torque control achieving the airgap flux limit at 1800 rpm.

VIII. CONCLUSION

This paper presents a control algorithm minimizing the total losses in a Dual-VSI DFIG-DC. The optimal conditions are derived analytically using Lagrange multipliers and validated with a numerical optimization package. They include an explicit expression for the optimal stator frequency vs speed profile and implicit conditions for the airgap flux and d-axis stator/rotor current split. The optimized control is built around a FOC core based on the airgap flux and sets the optimal stator frequency, airgap flux and d-axis stator/rotor current split for given speed and torque values. As main novelties with respect to the existing literature, the proposed approach includes core and VSI losses in the optimization and implements the implicit optimal flux condition using a dedicated PI controller, without look-up tables or iterative solution of non-linear equations. The implementation in the test-rig is realized using two independent, low-cost, DSPs in charge of the stator and rotor VSI control respectively and with no communication between each other.

APPENDIX I

WRIM ratings: 3.2 kW, 4-pole, 380/110 V, 8.1/19 A. Per-unit parameters of WRIM and VSIs: r_s=0.06, r_r =0.05, L_m=1.5, L_{ks}=0.10, L_{kr}=0.10, p_{se0}=0.015, p_{sh0}=0.007, p_{re0}=0.013, p_{rh0}=0.005, p_{invs0}=0.04, p_{invr0}=0.04. Base values: S_B=5350 VA, f_B=50 Hz, U_B= 380 V, T_B=34 Nm. The WRIM core losses were obtained from several no-load tests both at standstill (short-circuited rotor) and with open-rotor driven at synchronism via an external drive. The method of loss separation described in [24] was used.

APPENDIX II

Switching losses calculation in the VSI: According to [26] and [27] switching losses in VSI at a terminal current I_0 can be approximated by:

$$P_{sw} = \frac{1}{2}U_{dc}I_0 f_{sw}\left(t_r + t_f\right) = f_{sw}\left(W_{on} + W_{off}\right) \quad \text{(AII-1)}$$

where the switching characteristics of IGBTs W_{on} and W_{off} are given in their datasheets. Considering an approximately constant sum of the turn-on and turn-off times $\left(t_r + t_f\right)$ and assuming a constant dc-voltage level result in semiconductor switching losses proportional to current.

In this work, switching losses were therefore lumped into expressions (8)-(9) along with conduction losses. The contribution of switching losses coefficients $P_{inv_{s0}}$ and $P_{inv_{r0}}$ were computed for rated current and dc voltage using (AII-1) and parameters from datasheets. A more detailed explanation can be found in [17].

REFERENCES

[1] R. Cárdenas, R. Peña, S. Alepuz, G. Asher, "Overview of control systems for the operation of DFIGs in wind energy applications," *IEEE Trans. Ind. Electron.*, vol. 60, no. 7, pp. 2776–2798, July 2013.

[2] N. Holtsmark, H. J. Bahirat, M. Molinas, B. A. Mork, H. K. Hoidalen, "An All-dc Offshore Wind Farm With Series-Connected Turbines: An Alternative to the Classical Parallel AC Model?" *IEEE Trans. Ind. Electron.*, vol. 60, no. 6, pp. 2420-2428, June 2013.

[3] H. Kakigano, Y. Miura, T. Ise "Low-voltage bipolar-type dc microgrid for super high quality distribution," *IEEE Trans. Power Electron.*, vol. 25, no. 12, pp. 3066-3075, Dec. 2010.

[4] T. Dragičević, X. Lu, J. C. Vasquez and J. M. Guerrero, "DC Microgrids—Part I: A Review of Control Strategies and Stabilization Techniques," *IEEE Trans. Pow. Electron.*, vol. 31, no. 7, pp. 4876-4891, July 2016.

[5] G. D. Marques, M. F. Iacchetti, "DFIG topologies for DC networks: a review on control and design features," *IEEE Trans. Pow. Electron.*, vol. 34, no. 2, pp. 1299-1316, Feb. 2019.

[6] C. Wu, H. Nian, "An Improved Repetitive Control of DFIG-DC System for Torque Ripple Suppression," *IEEE Trans. Pow. Electron.*, vol. 33, no. 9, pp. 7634-7644, Sept. 2018.

[7] J. Hu, H. Nian, H. Xu, and Y. He, "Dynamic modeling and improved control of DFIG under distorted grid voltage conditions," *IEEE Trans.Energy Convers.*, vol. 26, no. 1, pp. 163–175, Mar. 2011.

[8] H. Nian, X. Yi, "Coordinated control strategy for doubly-fed induction generator with dc connection topology," *IET Renew. Power Gener.*, vol. 9, no. 7, pp. 747–756, Aug. 2015.

[9] Y. Kawabata, E. Ejiogu and T. Kawabata, "Vector-controlled double-inverter-fed wound-rotor induction motor suitable for high-power drives," *IEEE Trans. Ind. Appl.*, vol. 35, no. 5, pp. 1058-1066, Sep/Oct 1999.

[10] F. Bonnet Francois, P. E. Vidal and M. Pietrzak-David, "Dual Direct Torque Control of Doubly Fed Induction Machine," *IEEE Transactions on Industrial Electronics*, vol. 54, no. 5, pp. 2482-2490, Oct. 2007.

[11] M. Abdellatif, M. Debbou, I. Slama-Belkhodja, and M. Pietrzak-David, "Simple Low-Speed Sensorless Dual DTC for Double Fed Induction Machine Drive," *IEEE Trans. on Ind. Electron.*, vol. 61, pp. 3915-3922, 2014.

[12] G. Poddar and V. T. Ranganathan, "Direct-torque and frequency control of double-inverter-fed slip-ring induction motor drive," *IEEE Trans. Ind. Electron.*, vol. 51, no. 6, pp. 1329-1337, Dec. 2004.

[13] G. Poddar and V. T. Ranganathan, "Sensorless double-inverter-fed wound-rotor induction-Machine drive," *IEEE Trans. Ind. Electron.*, vol. 53, no. 1, pp. 86-95, Feb. 2006.

[14] N. K. Bajjuri, A. K. Jain, "Torque Ripple Reduction in Double-Inverter fed Wound Rotor Induction Machine Drives using PWM techniques," in *IEEE trans Ind. Electron*., vol. 66, no. 6, pp. 4250-4261, June 2019.

[15] Yifan Tang and Longya Xu, "A flexible active and reactive power control strategy for a variable speed constant frequency generating system," in IEEE Transactions on Power Electronics, vol. 10, no. 4, pp. 472-478, July 1995.

[16] B. Rabelo, W. Hofmann, and L. Pinheiro, "Loss reduction methods for doubly-fed induction generator drives for wind turbines," in *Proc. Int. Symp. Power Electron., Elect. Drives, Autom. Motion*, 2006,.

[17] B. Zhang, W. Hu, and Z. Chen, "Loss minimizing operation of doubly fed induction generator based wind generation systems considering reactive power provision," in *Proc. 40th Annu. Conf. IEEE Ind. Electron. Soc.*, 2014, pp. 2146–2152.

[18] J. Gillet, M. P. David and F. Messine, "Optimization of the control of a doubly fed induction machine," *IEEE 11th Int. Work. Electron., Contr., Meas., Sign. & Appl.Mechatron.*, Toulouse, 2013, pp. 1-5.

[19] G. D. Marques, M. F. Iacchetti, "Field Weakening Control for Efficiency Optimization in a DFIG connected to a dc Link" *IEEE Trans. Ind. Electron.*, Vol. 63, No.6, pp. 3409 – 3419, June. 2016.

[20] S. M. A. Cruz, G. D. Marques, P. F. C. Gonçalves and M. F. Iacchetti, "Predictive Torque and Rotor Flux Control of a DFIG-DC System for Torque Ripple Compensation and Loss Minimization," *IEEE Trans. on Ind. Electron*, vol. 65, no. 12, pp. 9301-9310, Dec. 2018.

[21] S. Yan, A. Zhang, H. Zhang, J. Wang, B. Cai, "Optimized and coordinated model predictive control sheme for DFIGs with DC-Based converter system," *J. Mod. Power Syst. Clean Energy*, 5: 620, 2017.

[22] S. Yan, A. Zhang, H. Zhang and J. Wang, "Control scheme for DFIG converter system based on DC-transmission," in *IET Electric Power Applications*, vol. 11, no. 8, pp. 1441-1448, 9 2017.

[23] Y. Han and J. I. Ha, "Control Method of Double Inverter Fed Wound Machine for Minimizing Copper Loss in Maximized Operating Area," *IEEE Trans. on Ind. Electron.*, vol. 64, no. 10, pp. 7700-7710, Oct. 2017.

[24] M. G. Say, "Alternating Current Machines", 4nd ed. Pitman & Sons, Ltd. London (1978), p-346-348.

[25] M. N. Uddinand, S. W. Nam, "Newonlineloss-minimization-based control of an induction motor drive," *IEEE Trans. Power Electron.*, vol. 23, no. 2, pp. 926–933, Mar. 2008.

[26] Mohan, Undeland, Robins, "Power Electronics, Converters, Applications and Design" Wiley, Second Edition (1995), p-23.

[27] José Fernando Silva, "Electrónica Industrial – Semicondutores e Conversores de Potência", Fundação Calouste Gulbenkian, (2013), p-97.